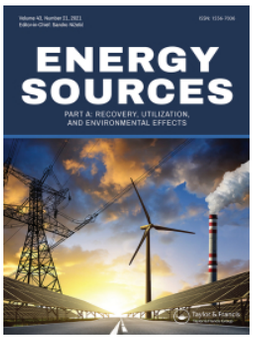

Taylor & Francis
Taylor & Francis Group

Energy Sources, Part A: Recovery, Utilization, and Environmental Effects

ISSN: (Print) (Online) Journal homepage: www.tandfonline.com/journals/ueso20

Numerical modeling and analysis of FeS_2-based solar cell employing $CuBi_2O_4$ as back surface field layer

Md. Shah Kamal, Sheikh Shehab Uddin, Fahmid Kabir, Md. Fakhrul Alam, Md. Atikur Rahman & Md. Habibur Rahman

To cite this article: Md. Shah Kamal, Sheikh Shehab Uddin, Fahmid Kabir, Md. Fakhrul Alam, Md. Atikur Rahman & Md. Habibur Rahman (2024) Numerical modeling and analysis of FeS_2-based solar cell employing $CuBi_2O_4$ as back surface field layer, Energy Sources, Part A: Recovery, Utilization, and Environmental Effects, 46:1, 12901-12912, DOI: 10.1080/15567036.2024.2402924

To link to this article: https://doi.org/10.1080/15567036.2024.2402924

Published online: 13 Sep 2024.

ENERGY SOURCES, PART A: RECOVERY, UTILIZATION, AND ENVIRONMENTAL EFFECTS
2024, VOL. 46, NO. 1, 12901–12912
https://doi.org/10.1080/15567036.2024.2402924

Numerical modeling and analysis of FeS_2-based solar cell employing $CuBi_2O_4$ as back surface field layer

Md. Shah Kamal [a], Sheikh Shehab Uddin [b], Fahmid Kabir [b], Md. Fakhrul Alam [c], Md. Atikur Rahman [a], and Md. Habibur Rahman [a]

[a]Department of Electrical & Electronics Engineering, University of Dhaka, Dhaka, Bangladesh; [b]Institute of Energy, University of Dhaka, Dhaka, Bangladesh; [c]Department of Electrical Electronic & Communication Engineering, Military Institute of Science & Technology (MIST), Dhaka, Bangladesh

ABSTRACT

This research explores a novel design for thin-film solar cells, featuring FeS_2 as the absorber layer, $CuBi_2O_4$ as the back surface field (BSF) layer, and GaAs as the buffer layer. We carefully evaluate the solar cell's performance using the SCAPS 1D simulator, including layer thickness, doping levels, and FeS_2 and $CuBi_2O_4$ defect concentrations. Our n-GaAs/p- FeS_2 solar cell exhibits a notable power conversion efficiency (PCE) of 19.19%, a J_{SC} of 46.34 mA/cm^2, a V_{OC} of 0.517 V, and an FF of 80.02%. However, our study delves deeper into the intriguing introduction of the $CuBi_2O_4$ BSF layer as a second absorber layer in solar cells. This modification boosts PCE to 33.29%, J_{SC} (49.64 mA/cm^2), and V_{OC} (0.843 V) while retaining a high FF of 79.58%. The proposed FeS_2/$CuBi_2O_4$ structure represents an impressive 73.49% improved cell performance compared to the conventional single junction FeS_2-based solar cell. Due to the excellent band alignment in the dual-heterojunction arrangement, the efficiency increases significantly. Our study advances FeS_2 solar cell optimization, showing the promise of innovative material combinations for photovoltaic technology. Our findings also highlight the importance of adding second absorber layers to improve solar cell efficiency and contribute to sustainable energy.

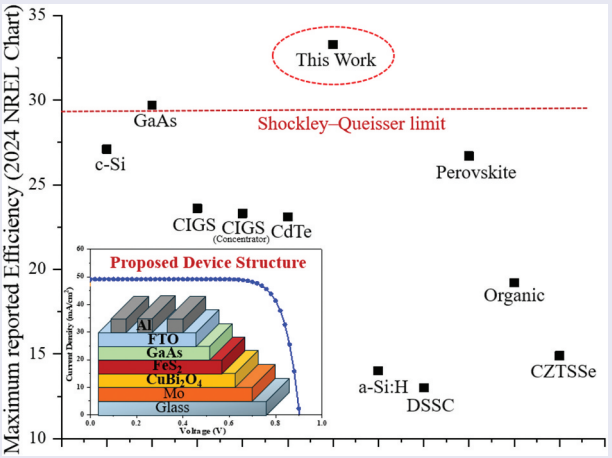

ARTICLE HISTORY

Received 25 May 2023
Revised 8 August 2024
Accepted 10 August 2024

KEYWORDS

Back surface field; $CuBi_2O_4$; FeS_2; SCAPS 1D; thin film solar cell

CONTACT Md. Shah Kamal mdshahkamal-2013012407@eee.du.ac.bd Department of Electrical & Electronics Engineering, University of Dhaka, Dhaka 1000, Bangladesh

Introduction

The topic of climate change has brought about a significant emphasis on renewable energy sources, particularly solar photovoltaics (PV). It is worth noting that the energy from the sun that reaches the earth's surface within an hour alone can satisfy the entire global energy demand for a year (Quaschning 2019) (Bhuiyan et al. 2021). Compared to Si solar cells, thin film solar cells (TFSCs) have gained popularity because of their low cost, simple construction method, and equivalent efficiency. CZTS-based solar cells are popular among different TFSCs due to their availability and low toxicity (Efaz et al. 2021). Introducing Cu_2ZnSnS_4 (CZTS) was considered a favorable option for researchers. This is due to its high optical absorption coefficient of over 10^4 cm^{-1}, enabling it to capture roughly 90% of the incoming solar photons (Grossberg et al. 2019). Additionally, CZTS has an adjustable energy band gap of approximately 1.4–1.6 eV, which closely aligns with the optimal energy bandgap of single junction solar cells (Jhuma, Shaily, and Rashid 2019). Iron pyrite (FeS_2) has been acknowledged as a highly efficient absorber material for TFSCs, mainly due to its distinctive electrical and optical properties. Iron disulfide (FeS_2) is inexpensive and abundant, which could reduce solar cell manufacturing costs (Wadia, Alivisatos, and Kammen 2009). FeS_2 greatly absorbs visible and infrared lights. FeS_2's broad absorption spectrum efficiently gathers a wide range of wavelengths, improving the solar cell energy conversion efficiency. FeS_2's straight bandgap makes it ideal for solar applications. The high absorption coefficient of FeS_2 is proportional to the thin film's thickness, allowing complete light absorption, a bandgap of 0.95 eV, and long minority carrier diffusion lengths (100–1000 nm). Because FeS_2 is abundant, it minimizes the need for expensive and rare parts in typical solar cells, promoting sustainability (Schieck et al. 1990). The use of FeS_2 in tandem solar cells, which combine multiple layers of materials to boost efficiency, shows its adaptability and potential. Despite its potential, efficiency and scalability issues are being addressed through research and development. FeS_2 is intriguing and promising for solar energy conversion due to its unique and sustainable features (Voigt et al. 2019).

$CuBi_2O_4$ is a low-cost, easy-to-use photocathode material for solar cells (Sullivan, Zoellner, and Maggard 2016) (Elaziouti et al. 2015). Moreover, it is nontoxic, abundant and has a low band gap of 1.4 to 1.8 eV and a high optical absorption coefficient of ~10^4 cm^{-1}, making it suitable for solar photovoltaic devices (Wang et al. 2017). When integrated into solar cell topologies, a back surface field (BSF) layer is typically utilized to decrease the width of the valence band barrier and minimize recombination losses at the back surface (Hosen et al. 2024) (Song et al. 2019). The BSF layer increases efficiency and Fill Factor by reducing shunting in the absorber layer (Kazmi et al. 2020). Also, thin-film solar cells with a second absorber layer like $CuBi_2O_4$ show potential for PV technology. This novel strategy has many benefits. First, it increases the solar cell's light absorption capacity, allowing it to collect more wavelengths and increase efficiency. This method efficiently converts a larger photon energy range into tandem solar cells with multiple absorber layers and band gaps. The intentional integration of a second absorber layer reduces solar cell thickness while preserving efficiency, which is important for lightweight and flexible solar applications. The adaptability of this method allows for customized designs for certain applications and environments.

This study aims to investigate the significance of BSF in the context of FeS_2-based thin-film solar cells and employs the utilization of $CuBi_2O_4$ as a secondary absorber layer. The FeS_2-based thin film solar cell structure configuration was Al/FTO/n-GaAs/p-FeS_2/p^+-$CuBi_2O_4$/Mo. By optimizing FeS_2/$CuBi_2O_4$ layer thickness, doping level, defect concentration, and temperature, a 33.29% efficiency with a high 0.843 V open-circuit voltage was obtained. The study essentially seeks to improve PV technology by improving FeS_2-based solar cell understanding and exploring new material combinations.

Device layout and simulation methods

This study examined the PV performance of a heterojunction solar device with Al/FTO/n-GaAs/p-FeS_2/p^+-$CuBi_2O_4$/Mo/rigid glass substrate. The proposed structure and associated band diagram of

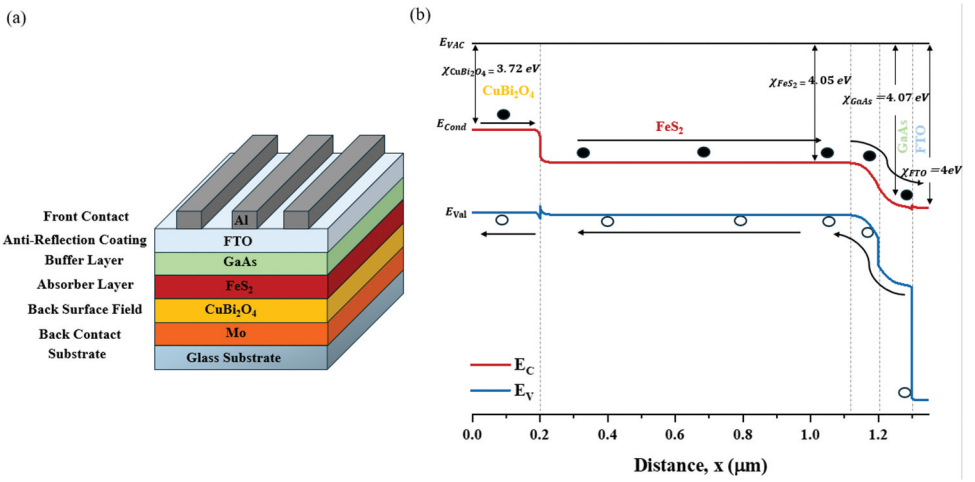

Figure 1. Schematic (a) and band diagram (b) of the proposed $FeS_2/CuBi_2O_4$ based solar cell structure.

the FTO/GaAs/FeS_2/$CuBi_2O_4$ structure are illustrated in Figure 1. FeS_2 has a lattice parameter of 5.4195 Å, a band gap of 0.95 eV, and an electron affinity of 4.0 eV (Hossain, Mondal, and Mostaque 2022). In contrast, GaAs have a lattice parameter of 5.653 Å, a band gap of 1.424 eV, and an electron affinity of 4.07 eV (Kayali). Thus, the closely matched lattice parameters of FeS_2 and GaAs will reduce the defects at their interfaces. $CuBi_2O_4$ is a suitable BSF layer for the FeS_2 absorber layer due to its good band alignment (1.4 to 1.8 eV), high absorption coefficient, and preferable lattice parameters (5.814 Å and 5.823 Å) (Hosen, Mian, and Ahmed 2021). The formation of a pp^+ junction between the $CuBi_2O_4$ layer and the FeS_2 layer results in an upward switching of the valence band maximum. This switching is attributed to the high built-in potential generated at the interface due to the higher doping in the BSF layer. Consequently, a minor steep rise occurs at the interface, facilitating the easy traversal of holes. Previous research has shown that adjusting the back contact metal's work function within the range of 4.5 to 5.5 eV, with particular emphasis on 4.9 eV (Hosen et al. 2024), significantly improves solar cell properties, including Fill factor (FF), open-circuit voltage (V_{OC}), and overall cell performance (Sarker et al. 2023) (Hosen, Mian, and Ahmed 2021). This improvement was attributed to establishing an ohmic contact rather than a Schottky contact, which enhanced hole transportation within the solar cell (Hosen et al. 2024). To achieve high efficiency in $CuBi_2O_4$-based solar cells, a rear electrode with a work function exceeding 4.9 eV is essential (Michaelson 1977), with metals like Mo chosen for their optical properties and low resistivity, contributing to enhanced device performance (Chavan and Chaure 2019). The FeS_2-based TFSC structure was simulated using SCAPS 1D software under 100 mW/cm^2 incident power density of AM 1.5 G. All physical properties employed in the simulation are listed in Table 1.

Results and discussion

In Figure 2, the J-V characteristics of conventional and $FeS_2/CuBi_2O_4$ absorber cells exhibit V_{OC} dominance. Bilayer absorber construction increases V_{OC} by 62.97% compared to conventional structure from 0.517 V to 0.8426 V. Adding $CuBi_2O_4$ improved short circuit current (J_{SC}) from 46.349 mA/cm^2 to 49.64 mA/cm^2 (7.1% improvement) and efficiency from 19.1881% to 33.29% (73.49% improvement). Thus, increased J_{SC} also increases the V_{OC} as it is proportional to the generated photocurrent (J_{ph}) due to the absorber producing electron–hole pairs.

$CuBi_2O_4$ BSF layer beneath FeS_2 in the solar cell structure serves multiple purposes and provides significant advantages. First, it acts as an antireflection layer, helping to minimize light reflection at the

Table 1. Parameters of n-GaAs/p-FeS_2/p±$CuBi_2O_4$ solar cell.

Parameters	FTO (Kumar et al. 2020)	n GaAs (Lab 0000)	p FeS_2 (Hossain, Mondal, and Mostaque 2022)	p+ $CuBi_2O_4$ (Hosen, Mian, and Ahmed 2021)
Layer type	ARC/Window	Buffer	Absorber	BSF
*Thickness [μm]	0.05	0.1	1	.2
Band gap, E_G [eV]	3.5	1.424	.95	1.5
Electron affinity, χ [eV]	4	4.07	4.05	3.72
Dielectric permittivity, ε [relative]	9	12.9	1.9	34
Effective CB density, N_C [cm^{-3}]	2.2×10^{18}	4.7×10^{17}	3.0 × 1018	1.2 × 1019
Effective VB density, N_V [cm^{-3}]	1.8×10^{19}	9×10^{18}	3.0 × 1019	5 × 1019
Hole mobility, μ_p [$cm^2\ V^{-1}\ s^{-1}$]	10	400	70	1.2 × 10−3
Electron mobility, μ_n [$cm^2\ V^{-1}\ s^{-1}$]	20	8500	370	1.1 ×10−3
*Acceptor concentration, N_A. [cm^{-3}]	0	0	1.0 × 1017	3.7× 1018
*Donor concentration, N_D. [cm^{-3}]	1.0×10^{18}	1.0×10^{17}	0	0
Defect type	–	Acceptor	Donor	Donor
Energetic distribution	–	Gaussian	Gaussian	Gaussian
*Peak defect density, N(t) [$eV^{-1}\ cm^{-3}$]	–	1.0×10^{14}	1.0 × 1012	1.0 × 1012
Characteristic energy [eV]	0.1	0.1	.1	.1
Reference energy [eV]	0.6	0.6	.6	.6
Hole capture cross section for acceptor defect [cm^2]	1.0×10^{-15}	1.0×10^{-15}	1.0 × 10−15	1.0 × 10−15
Electron capture cross section for acceptor defect [cm^2]	1.0×10^{-15}	1.0×10^{-15}	1.0 × 10−15	1.0 × 10−15
Lattice Constant, (Å)	–	5.653	5.416	5.814

*The variable values.

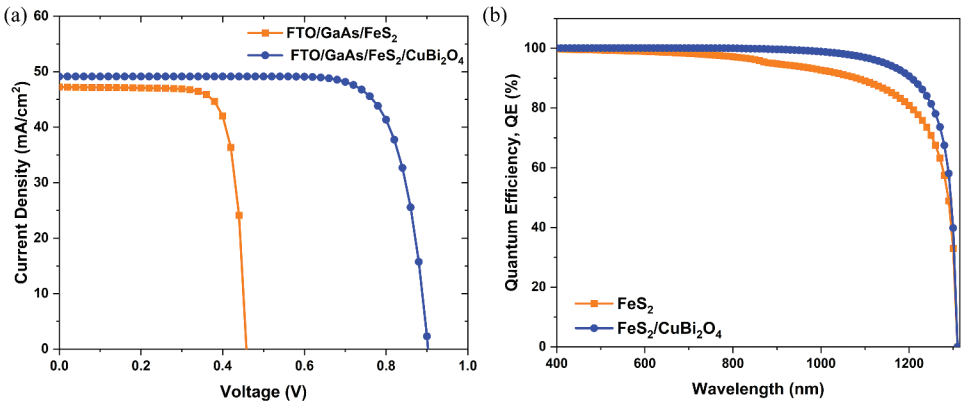

Figure 2. J-V characteristics (a) and spectral response (b) of the conventional and proposed structure.

back surface of the cell. This is evident from the increase in the J_{SC} , indicating that more incident light is effectively captured and converted into electricity. $CuBi_2O_4$ could serve primarily as a BSF layer, which helps to reduce recombination at the rear surface of the solar cell and improve charge carrier collection. This effect can contribute to both V_{OC} and J_{SC}. Moreover, introducing $CuBi_2O_4$ may lead to a band alignment phenomenon at the interface with the underlying solar cell layers, enhancing V_{OC}. Optimized band alignments can reduce recombination and improve charge carrier separation, resulting in higher V_{OC} (Barman and Kalita 2021). This band alignment effect can be supported by the observation that an increase in the doping concentration of the BSF layer enhances both J_{SC} and V_{oc} (Attafi et al. 2021). In addition, the J_{SC} is also directly influenced by the quantum efficiency (Eq. 1) (Kabir et al. 2022). The J-V characteristics and the quantum efficiency as a function of the wavelength (λ) are presented in Figure 2.

$$J_{SC} = \frac{q\lambda}{hc}\int S(\lambda)QE(\lambda)d\lambda \quad (1)$$

where q is election charge, h is Planck's constant, c is the speed of light in a vacuum, and QE (λ) is quantum efficiency, which is a measure of a solar cell's ability to convert photons at a specific wavelength into an electrical current, and S(λ) represents the intensity of the solar spectrum. The band diagram (Figure 1b) explains the small change in J_{SC}. A $FeS_2/CuBi_2O_4$ contact has valence band offset (VBO) and conduction band offset (CBO) values of 0.045 eV and 0.595 eV, respectively. In the presence of a VBO (which creates a barrier for the hole), the FeS_2 and $CuBi_2O_4$ layers may experience backflow due to band bending downhill (shown in Figure 1b), which can affect the hole mobility. This reverse conveyance of holes plays a crucial role in the slight variation of J_{SC}.

Effect of thicknesses of FeS_2 and $CuBi_2O_4$ layers

The thickness of the semiconductor material directly influences a solar cell's efficiency. Increased thickness of materials leads to enhanced absorption of light, particularly for longer wavelengths, hence leading to a greater value of J_{SC}. Additionally, they offer an increased capacity for charge carriers, enhancing the collection of carriers and resulting in higher values of V_{OC} and FF. Nevertheless, using thicker materials might also increase the probability of carrier recombination, diminishing overall efficiency. Determining the most suitable thickness of a material is a crucial aspect of the design, as it necessitates a careful equilibrium between maximizing light absorption and minimizing recombination. Moreover, factors such as cost and practicality must be taken into account. It is important to note that various solar cell technologies and materials require specific thickness adjustments to attain optimal performance. The thickness of the FeS_2 layer varied from 100 to 2000 nm, and that of the $CuBi_2O_4$ layer varied from 100 to 1000 nm to keep doping concentrations at a minimum. Donor doping concentrations for FeS_2 and $CuBi_2O_4$ were set at 1.0×10^{17} cm^{-3} and 3.7×10^{18} cm^{-3}, respectively, while also ensuring that the total defect density remains constant 1.0×10^{12} cm^{-3} for FeS_2 and 1.0×10^{12} cm^{-3} for $CuBi_2O_4$. These are chosen to achieve a compromise between efficiency maximization and overall thin film solar cell thickness.

Figure 3 demonstrates that the performance parameters remain nearly constant regardless of variations in the thickness of the $CuBi_2O_4$ layer for each respective FeS_2 layer thickness. (Figures 3a-d) show that the $CuBi_2O_4$ layer contributes little to the overall surplus carrier collection for the solar cell structure. Thus, the thickness of the $CuBi_2O_4$ layer has no significant effect on the suggested structure's performance. The $CuBi_2O_4$ BSF layer is normally located at the rear and away from the light source. Its main function is to decrease the dispersing of incident light. The BSF layer offers favorable band alignment, promoting the separation of electron–hole pairs generated within the cell, thus reducing cell recombination. However, increasing the FeS_2 layer thickness further improves all PV performance characteristics.

As indicated previously, V_{OC} and J_{SC} variations relate to the FF and efficiency variance, as seen in (Figures 3c,d). Because FF and V_{OC} are closely related, and FF changes at the same pace as V_{OC}. The relationship between FF and V_{oc} can be explained using the following I-V equation or Shockley Quasier equation (Eq. 2) (Barman and Kalita 2021) and FF equation (Eq. 3) (Kabir, Sakib, and Uddin 2019) in the context of solar cells.

$$J_{SC} = J_{ph} - J_0\left(e^{\frac{qV_{OC}}{kT}} - 1\right) \quad (2)$$

And,

$$FF = \frac{V_{max} \times I_{max}}{V_{oc}I_{sc}} \quad (3)$$

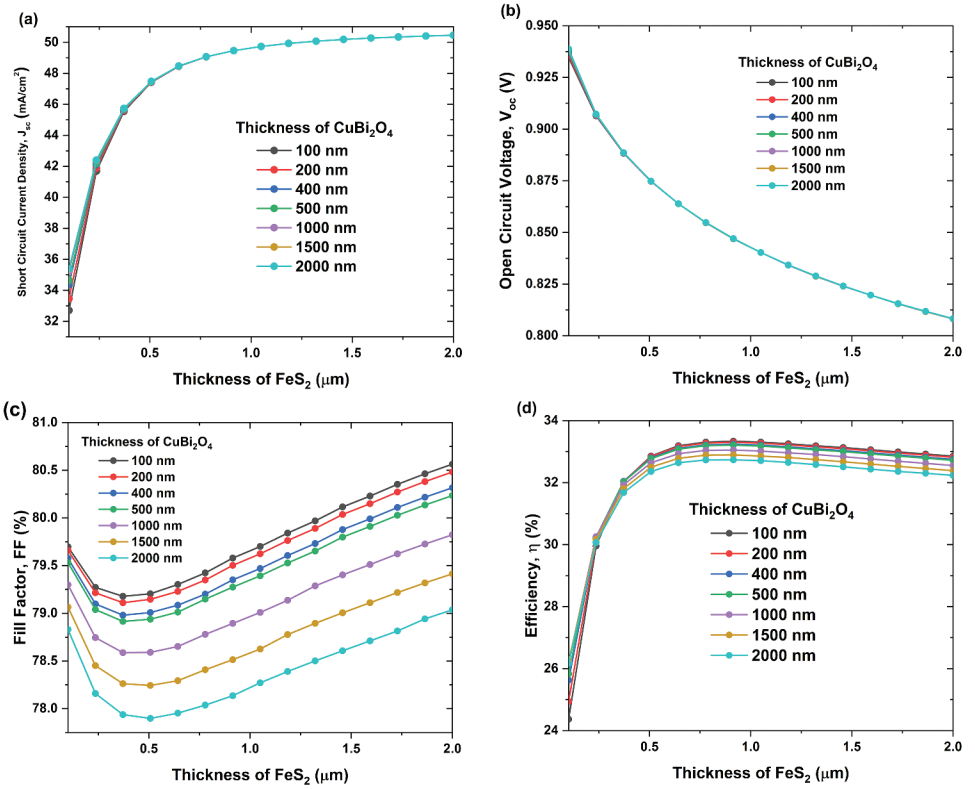

Figure 3. Effect of variation of thickness on (a) short circuit current density (J_{SC}), (b) open circuit voltage (V_{OC}), (c) fill factor (FF) and (d) efficiency (%η).

Where J_{ph}= generated photocurrent due to light absorption, J_0= reverse saturation current/dark current/leakage current in the absence of light, V_{OC} is the solar cell voltage, k is Boltzmann's constant, T is the temperature in Kelvin, and P_{max} (= $V_{max} \times I_{max}$) is the solar cell's maximum power output. The Shockley diode equation relates to V_{OC} and FF. V_{OC} changes may increase FF because the solar cell operates closer to its maximum power point (MPP), indicating improved efficiency. As voltage output increases, the solar cell's operating point approaches V_{MPP}, maximizing power conversion efficiency. This alignment leads to a proportional rise in FF, signifying improved utilization of available light energy. Changes in V_{OC} cause similar shifts in FF, emphasizing the symbiotic nature of these parameters in solar cell optimization and the importance of voltage in increasing power production and efficiency. Solar cell FF is frequently the hardest metric to optimize due to its sensitivity to parasitic loss processes. Solar cell V_{OC} determines the FF upper limit (Green 1982). Series (R_s) and shunt (R_{sh}) resistances lower the practical device FF. As Rs increases, the maximum power-point voltage drop ($V_{mpp} \times R_S$) lowers the power generating voltage. Quality of materials and interfaces, solar cell structure design, and device performance can affect FF and V_{OC} (Leijtens et al. 2014) (Wu et al. 2017).

Most importantly, the $FeS_2/CuBi_2O_4$ bilayer structural efficiency increases from 24.24% at 100 nm of FeS_2 to 33.63% at 800 nm of FeS_2. Like all other performance factors, efficiency increases slowly with thickness. The efficiency drops from 33.63% to 32.14% when the FeS_2 layer thickness is increased from 800 to 2000 nm. As a result, the thickness of the FeS_2 layer was kept at 800 nm thick for the proposed configuration. The $CuBi_2O_4$ layer was also tuned at 200 nm thickness due to its invariant influence on the solar cell performance with thickness variation. The GaAs buffer layer thickness affected the efficiency of the proposed structure; hence, 100 nm was chosen as the thinnest buffer layer available.

Effect of doping concentration of absorber layer

The deliberate introduction of impurities into a semiconductor material, known as doping concentration, has a substantial influence on the efficiency of solar cells. Appropriate doping regulation can augment the mobility of charge carriers, boost the band structure, and mitigate recombination, facilitating heightened efficiency. Doping is employed to modify the material's bandgap to enhance light absorption, particularly in multi-junction solar cells. Nevertheless, the overuse of doping can lead to undesirable consequences, such as the occurrence of parasite absorption and a decrease in transparency. Hence, the optimization of doping concentration plays a pivotal role in achieving a harmonious equilibrium among these parameters and maximizing the total efficiency of the solar cell. The absorber layer's doping concentration regulates carrier collection. The depletion zone width between layers in a p-n junction solar cell, which facilitates the movement of photogenerated carriers, is determined by the layer doping concentrations. The expansion of the depletion width (W) occurs toward the region of low doping concentration by a thermal equilibrium formulation, indicating that,

$$W = \sqrt{\frac{2 \in V_{bi}}{q}\left(\frac{N_D + N_A}{N_D N_A}\right)} \tag{4}$$

V_{bi} represents the built-in potential, and the other symbols used in the equation have also been previously defined. Neglecting the tiny dielectric constant differences between materials from Eq. 4 can also be employed for heterojunction. The doping concentrations of FeS_2 and $CuBi_2O_4$ were also varied to investigate how the doping concentration affected the performance of the $FeS_2/CuBi_2O_4$ structure.

(Figure 4a) demonstrates that for all FeS_2 doping levels, the J_{SC} increases with the increase of $CuBi_2O_4$ layer doping concentration but remains constant for $CuBi_2O_4$ doping density at 3.7×10^{19} cm^{-3} to 3.7×10^{20} cm^{-3}. (Figure 4b) shows that for both FeS_2 and $CuBi_2O_4$, the V_{OC} slightly increases with increasing doping density. The doping density of $CuBi_2O_4$ increased from 3.7×10^{16} cm^{-3} to 3.7×10^{20} $cm^{-3,}$ resulting in only minor variations at 0.841 V. The FF increases with the increase of $CuBi_2O_4$ doping concentration and peaks at 3.7×10^{20} cm^{-3} doping level. Similar patterns can be observed in the efficiency of bilayer structures. The increase in $CuBi_2O_4$ doping concentration intensifies the electric field and thus increases the structure's efficiency. The most optimal performance of the proposed $FeS_2/CuBi_2O_4$ bilayer structure achieved PCE of 33.29% for the doping concentrations of FeS_2 at 10^{19} cm^{-3} and $CuBi_2O_4$ at 3.7×10^{18} cm^{-3}, respectively, with $J_{SC} = 49.64$ mA/cm^2, $V_{OC} = 0.842$ V, and FF = 79.58%.

Effect of bulk defect density

Semiconductor defect density greatly affects the overall solar cell efficiency. The presence of imperfections within a material's crystal lattice can serve as sites that capture charge carriers produced through the absorption of sunlight. Recombination reduces the number of charge carriers available for electric current generation. Loss of recombination lowers the solar cell efficiency. High defect densities lower V_{OC} and FF, affecting the cell's ability to generate voltage and transfer power into electrical output. Neutral defects were introduced into the bilayer structure to evaluate how the absorber layer's defect states affect the proposed structure's performance. The defect state density ranged from 10^{15} cm^{-3} to 10^{20} cm^{-3} in both FeS_2 and $CuBi_2O_4$ layers. Figure 5 shows variations of different photovoltaic parameters varying with defect state density of FeS_2 and $CuBi_2O_4$ layers. All cell metrics decrease with increasing defect state density in the FeS_2 layer regardless of the $CuBi_2O_4$ layer. The efficiency is practically equal to zero for a bulk FeS_2 layer with a defect state density of 10^{20} cm^{-3}. Therefore, it is crucial to keep the density of defect states in the bulk FeS_2 layer to a minimum to improve cell performance. Interestingly, there was no significant change in the $CuBi_2O_4$ defect state density, and all the lines representing different levels of $CuBi_2O_4$ defect state density overlapped in Figure 5.

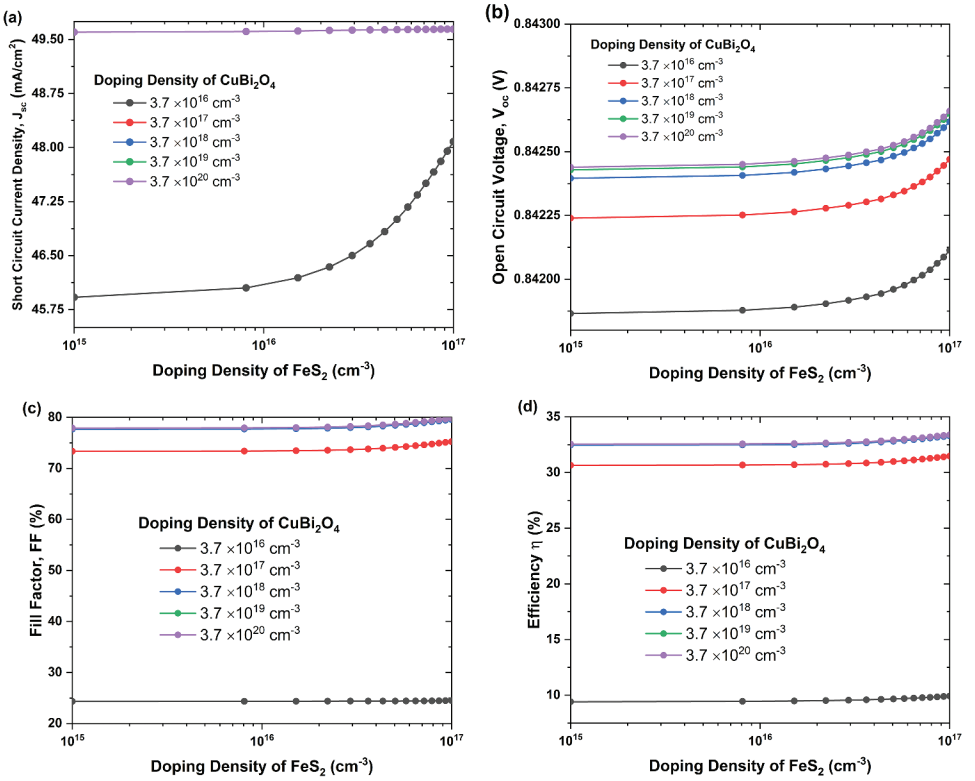

Figure 4. Effect of variation of doping concentration on (a) short circuit, J_{SC}, (b) open circuit voltage, V_{OC}, (c) fill factor, FF and (d) efficiency, η.

Effect of temperature

Solar cell performance is influenced by temperature. In semiconductors, temperature increases the charge carrier velocity, lowering the bond energy. This decreased bond energy narrows the band gap of semiconductors, which impacts the intrinsic carrier concentrations. The saturation current of the solar cell increases as inherent carriers grow. As shown in Figure 5, the suggested solar cell performs best between 300 K and 450 K. As seen in the diagram, the J_{SC} of the cell is independent of temperature. As the temperature increases, the reverse saturation current of the solar cell increases, causing a significant decrease in the V_{OC} of the solar cell. FF, however, varies significantly with temperature. At higher temperatures, photocarriers are more likely to collide with vibrating atoms, which may result in a solar cell's power loss.

Optimized cell performance of FeS_2-Based structure

The J-V characteristics of FTO/GaAs/FeS_2 and FTO/GaAs/FeS_2/$CuBi_2O_4$ solar cells are represented in Figure 2, while the device performance of the optimized solar cells is displayed in Table 2. The $CuBi_2O_4$ BSF layer boosts the solar cell's J_{SC} significantly. Thus, the significant increase in J_{SC} is due to longer wavelength and sub-bandgap photon absorption in the BSF layer.

The increase in V_{OC} with the BSF layer in a thin film solar cell is due to reduced recombination, improved charge carrier separation, and an enhanced electric field at the rear surface. As mentioned before, Voc and Jsc can also be interrelated in a thin film solar cell through the Shockley-Queisser equation (Eq. 3). V_{oc} affects J_{SC} indirectly through the exponential term in this

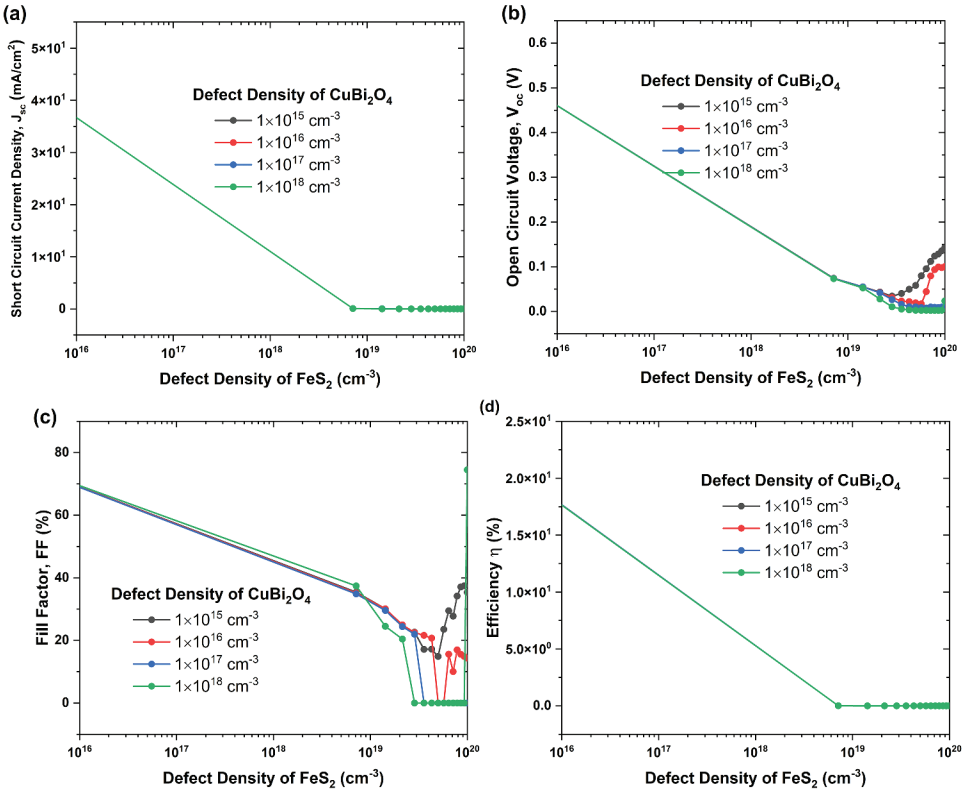

Figure 5. Effect of variation of defect doping concentration on (a) short circuit current density, J_{SC}, (b) open circuit voltage, V_{OC}, (c) fill factor, FF and (d) efficiency, η.

Table 2. Observed results for optimized FeS_2-based solar cells.

Parameters	FeS_2 Absorber Layer	$FeS_2/CuBi_2O_4$ Absorber Layer
Short Circuit Current Density, J_{sc} (mA/cm^2)	46.349	49.64
Open Circuit Voltage, V_{oc} (V)	0.517	0.8426
Fill Factor, FF (%)	80.0242	79.58
Efficiency (%)	19.1881	33.29

equation. An increase in V_{OC} results in a decrease in the exponential term, which, in turn, can lead to an increase in J_{SC}. However, balancing V_{OC} and J_{SC} is essential, as optimizing one may affect the other.

Band alignment between the absorber and BSF layers is crucial in a solar cell because it directly influences the V_{OC} and overall cell performance. The equation that relates the band alignment and V_{OC} in a solar cell is known as the Shockley-Read-Hall recombination equation (Eq.5)

$$V_{OC} = \frac{kT}{q} \ln\left(\frac{J_{ph}}{J_{ph} + J_0}\right) \tag{5}$$

The band alignment directly affects J_{ph}, which, in turn, influences V_{OC}. Optimizing band alignment ensures efficient charge separation and minimal recombination at the absorber–BSF interface, leading to a higher V_{OC} and better solar cell performance.

(Figure 2b) compares the QE of FTO/GaAs/FeS_2 and FTO/GaAs/FeS_2/$CuBi_2O_4$ solar cells. As seen in (Figure 2b), the $CuBi_2O_4$ BSF layer significantly changes the QE of the solar cell. Because

Table 3. Comparison of different types of solar cells.

Thin Film Solar Cell Structure	V_{OC} (V)	J_{SC} (mA/cm^2)	FF (%)	PCE (%)	Type	Year	Reference
Al/FTO/CdS/CIGS/$BaSi_2$/Mo	0.843	40.56	76.76	26.24	Simulation	2019	(Biplab et al. 2020)
ZnO/CdS/CdTe/NiO/Au	1.09	29.09	87.84	28.04	Simulation	2020	(Ahmmed et al. 2020)
ITO/CeO_2/SnS/NiO/Mo	0.89	32.67	86.19	25.10	Simulation	2020	(Ahmmed et al. 2020)
ITO/CeO_2/SnS/NiO/Mo	0.89	32.67	86.19	25.10	Simulation	2020	(Ahmmed et al. 2020)
ITO/*n-CdS/CdTe*/CdSe/Mo	0.889	28.33	84.90	21.29	Simulation	2021	(Kuddus, Ismail, and Hossain 2021)
ITO/*n-CdS/CdTe*/p^+-*CdSe*/CdSe/Mo	1.146	30.66	88.57	31.11	Simulation	2021	(Kuddus, Ismail, and Hossain 2021)
ITO/*n-CdS*/CdTe/p^+-Sb_2Se_3/CdSe/Mo	1.046	49.22	85.71	44.14	Simulation	2021	(Kuddus, Ismail, and Hossain 2021)
Mo/*n*-CdS/*p*-HPGe/p^+-$BaSi_2$/Al	1.16	46.84	83.87	45.56	Simulation	2021	(Hossain et al. 2021)
Mo/$CuBi_2O_4$/CdS/FTO/Al	0.97	31.61	84.58	26.0	Simulation	2021	(Hosen, Mian, and Ahmed 2021)
Au/$CuBi_2O_4$/WS_2/ITO	1.33	21.08	81.3	22.84	Simulation	2022	(Reddy et al. 2022)
Au/$CuBi_2O_4$/$SrSnO_3$/ITO	1.32	20.70	80.71	22.19	Simulation	2022	(Manjunath et al. 2022)
Ni/$CuBi_2O_4$/CdS/SnO_2/Al	1.37	25.85	86.5	31.41	Simulation	2022	(Lachhab et al. 2022)
Ni/$CuBi_2O_4$/CdS/SnO_2/Al	1.38	26.2	88.8	31.8	Simulation	2022	(Lachhab et al. 2022)
Mo/FeS_2/CdS/ZnO/AZO	0.5266	42.09	50.51	11.20	Simulation	2023	(Livingston et al. 2023)
Electrode/FeS_2/Surface inversion layer/FTO	0.36	41.9	67.11	10.28	Simulation	2023	(Gohri et al. 2023)
Mo/Cu_2O/$CuBi_2O_4$/CdS/FTO/Al	1.02	32.49	87.91	29.2	Simulation	2024	(Hosen et al. 2024)
Al/FTO/GaAs/FeS_2/$CuBi_2O_4$/Mo	0.842	49.64	79.59	33.29	Simulation		This Study

of the tail states in the $CuBi_2O_4$ BSF layer, the suggested solar cell's QE marginally increases from 800 to 1300 nm, increasing the J_{SC}. Table 3 compares CdTe, CIGS, Ge, GaAs, $CuBi_2O_4$, FeS_2, etc.

Conclusion

The potential of thin-film solar cell research in the future is highly promising, as breakthroughs in creative materials, design, scalable production methods, and environmental awareness. This study used the SCAPS 1D simulator to explore how thickness, doping concentration, and defect state density affect FeS_2/$CuBi_2O_4$ thin film-based solar cells. The proposed FeS_2/$CuBi_2O_4$ structure has a 33.29% efficiency, representing an impressive 73.49% increment compared to the conventional single junction FeS_2-based solar cell (19.19%). The $CuBi_2O_4$ layer reduced light reflection at the rear surface, recombination, and enhanced charge carrier collection, increasing J_{SC} by 7%. While J_{SC} saw notable improvement, the main contributor to the enhanced efficiency was the significant improvement in V_{OC}. The proposed FeS_2/$CuBi_2O_4$ structure significantly improved V_{OC} (0.84 V) by ~63% compared to FeS_2 solar cells (0.517 V). This elevation in V_{OC} directly results from the greater built-in potentials created at the interfaces between n-GaAs/p-FeS_2 and p-FeS_2/p^+- $CuBi_2O_4$, enabled by a favorable band alignment within the dual-heterojunction design. These combined advancements increased the efficiency of FeS_2-based solar cells and have the potential to unlock their full potential, contributing to future sustainable energy technology.

Acknowledgements

The authors thank Dr Marc Bargelman of the University of Gent in Belgium for offering SCAPS-1D software free of charge.

Disclosure statement

No potential conflict of interest was reported by the author(s).

Funding

The author(s) reported no funding associated with the work featured in this article.

ORCID

Md. Shah Kamal http://orcid.org/0009-0009-5352-6974
Sheikh Shehab Uddin http://orcid.org/0000-0003-3000-3678
Fahmid Kabir http://orcid.org/0000-0003-3998-2753

References

Ahmmed, S., A. Aktar, J. Hossain, and A. B. M. Ismail. 2020. Enhancing the open circuit voltage of the SnS based heterojunction solar cell using NiO HTL. *Solar Energy* 207:693–702. doi: 10.1016/j.solener.2020.07.003.

Ahmmed, S., A. Aktar, M. F. Rahman, J. Hossain, and A. B. M. Ismail. 2020. A numerical simulation of high efficiency CdS/CdTe based solar cell using NiO HTL and ZnO TCO. *Optik* 223:165625. doi: 10.1016/j.ijleo.2020.165625.

Attafi, D., R. Boumaraf, A. Meftah, and N. Sengouga. 2021. Effect of a back-surface field and passivation layer on a silicon schottky solar cell. *Transactions on Electrical and Electronic Materials* 22 (3):357–62. doi: 10.1007/s42341-020-00246-4.

Barman, B., and P. Kalita. 2021. Influence of back surface field layer on enhancing the efficiency of CIGS solar cell. *Solar Energy* 216:329–37. doi: 10.1016/j.solener.2021.01.032.

Bhuiyan, M. M. H., et al. 2021. Effect of combination of natural dyes and the blocking layer on the performance of DSSC. *Solar Cells-Theory, Materials and Recents Advance*.

Biplab, S. R. I., M. H. Ali, M. M. A. Moon, M. F. Pervez, M. F. Rahman, and J. Hossain. 2020. Performance enhancement of cigs-based solar cells by incorporating an ultrathin BaSi 2 BSF layer. *Journal of Computational Electronics* 19 (1):342–52. doi: 10.1007/s10825-019-01433-0.

Chavan, K., and N. B. Chaure. 2019. Studies on controlled preferentially orientated Mo thin films via sputtering technique. *Materials Research Express* 6 (7):076423. doi: 10.1088/2053-1591/ab162d.

Efaz, E. T., M. M. Rhaman, S. A. Imam, K. L. Bashar, F. Kabir, M. E. Mourtaza, S. N. Sakib, and F. A. Mozahid. 2021. A review of primary technologies of thin-film solar cells. *Engineering Research Express* 3 (3):032001. doi: 10.1088/2631-8695/ac2353.

Elaziouti, A., N. Laouedj, A. Bekka, and R.-N. Vannier. 2015. Preparation and characterization of p–n heterojunction CuBi2O4/CeO2 and its photocatalytic activities under UVA light irradiation. *Journal of King Saud University-Science* 27 (2):120–35. doi: 10.1016/j.jksus.2014.08.002.

Gohri, S., J. Madan, M. K. Mohammed, and R. Pandey. 2023. Inherent internal pn junction assisted single layered n-type iron pyrite solar cell. *Materials Research Express* 10 (2):024001. doi: 10.1088/2053-1591/acb982.

Green, M. A. 1982. Accuracy of analytical expressions for solar cell fill factors. *Solar Cells* 7 (3):337–40. doi: 10.1016/0379-6787(82)90057-6.

Grossberg, M., J. Krustok, C. J. Hages, D. M. Bishop, O. Gunawan, R. Scheer, S. M. Lyam, H. Hempel, S. Levcenco, T. Unold, et al. 2019. The electrical and optical properties of kesterites. *Journal of Physics: Energy* 1 (4):044002. doi: 10.1088/2515-7655/ab29a0.

Hosen, A., M. S. Mian, and S. R. A. Ahmed. 2021. Simulating the performance of a highly efficient CuBi 2 O 4-based thin-film solar cell. *SN Applied Sciences* 3 (5):1–13. doi: 10.1007/s42452-021-04554-z.

Hosen, A., S. Yeasmin, K. S. B. Rahmotullah, M. F. Rahman, and S. R. Al Ahmed. 2024. Design and simulation of a highly efficient CuBi2O4 thin-film solar cell with hole transport layer. *Optics and Laser Technology* 169:110073. doi: 10.1016/j.optlastec.2023.110073.

Hossain, J., B. K. Mondal, and S. K. Mostaque. 2022. Design of a highly efficient FeS2-based dual-heterojunction thin film solar cell. *International Journal of Green Energy* 19 (14):1531–42. doi: 10.1080/15435075.2021.2011291.

Hossain, J., M. M. A. Moon, B. K. Mondal, and M. A. Halim. 2021. Design guidelines for a highly efficient high-purity germanium (HPGe)-based double-heterojunction solar cell. *Optics and Laser Technology* 143:107306.

Jhuma, F. A., M. Z. Shaily, and M. J. Rashid. 2019. Towards high-efficiency CZTS solar cell through buffer layer optimization. *Materials for Renewable and Sustainable Energy* 8 (1):1–7. doi: 10.1007/s40243-019-0144-1.

Kabir, F., S. Manir, M. M. H. Bhuiyan, S. Aftab, H. Ghanbari, A. Hasani, M. Fawzy, G. L. T. De Silva, M. R. Mohammadzadeh, R. Ahmadi, et al. 2022. Instability of dye-sensitized solar cells using natural dyes and approaches to improving stability–an overview. *Sustainable Energy Technologies and Assessments* 52:102196. doi: 10.1016/j.seta.2022.102196.

Kabir, F., S. N. Sakib, and S. S. Uddin. 2019. Effect of MWCNT's concentration in TiO2 based DSSC and degradation study of the cell. *Journal of Renewable and Sustainable Energy* 11 (2). doi: 10.1063/1.5055725.

Kayali, S. GaAs material properties. https://parts.jpl.nasa.gov.

Kazmi, S. A. A., A. D. Khan, A. D. Khan, A. Rauf, W. Farooq, M. Noman, and H. Ali. 2020. Efficient materials for thin-film CdTe solar cell based on back surface field and distributed bragg reflector. *Applied Physics A* 126 (1):1–8. doi: 10.1007/s00339-019-3221-5.

Kuddus, A., A. B. M. Ismail, and J. Hossain. 2021. Design of a highly efficient CdTe-based dual-heterojunction solar cell with 44% predicted efficiency. *Solar Energy* 221:488–501. doi: 10.1016/j.solener.2021.04.062.

Kumar, M., A. Raj, A. Kumar, and A. Anshul. 2020. An optimized lead-free formamidinium Sn-based perovskite solar cell design for high power conversion efficiency by SCAPS simulation. *Optical Materials* 108:110213. doi: 10.1016/j.optmat.2020.110213.

Lab, B. Y. U.-I. M. Semiconductor properties. https://cleanroom.byu.edu/semiconductor-properties.

Lachhab, S., A. Bliya, H. Diyagh, S. Ouhssain, E. Al Ibrahmi, and L. Dlimi. 2022. Comparative evaluation of the numerical results carried out on the buffer layer in order to optimize the performance of the SnO2/CdS/CuBi2O4 structure. *Optik* 265:169406. doi: 10.1016/j.ijleo.2022.169406.

Lachhab, S. E., A. Bliya, H. Diyagh, H. En-Nkhili, H. Shindou, S. Ouhssain, H. Slimane, E. Al Ibrahmi, and L. Dlimi. 2022. Comparative evaluation of SnO2/CdS/CuBi2O4 structure performance based on SnO2 window layer numerical and experimental analysis. *Journal of the Indian Chemical Society* 99 (10):100699. doi: 10.1016/j.jics.2022.100699.

Leijtens, T., S. D. Stranks, G. E. Eperon, R. Lindblad, E. M. J. Johansson, I. J. McPherson, H. Rensmo, J. M. Ball, M. M. Lee, H. J. Snaith, et al. 2014. Electronic properties of meso-superstructured and planar organometal halide perovskite films: Charge trapping, photodoping, and carrier mobility. *Agricultural Science & Technology Nano* 8 (7):7147–55. doi: 10.1021/nn502115k.

Livingston, L. M., A. G. S. Raj, R. T. Prabu, and A. Kumar. 2023. Computational analysis of FeS2 material for solar cell application. *Optical and Quantum Electronics* 55 (3):244. doi: 10.1007/s11082-022-04531-9.

Manjunath, V., Y. K. Reddy, S. Bimli, R. J. Choudhary, and R. S. Devan. 2022. 22% efficient Kusachiite solar cells of CuBi2O4 light harvester and ABO3 buffer layers: A theoretical analysis. *Materials Today Communications* 32:104061. doi: 10.1016/j.mtcomm.2022.104061.

Michaelson, H. B. 1977. The work function of the elements and its periodicity. *Journal of Applied Physics* 48 (11):4729–33. doi: 10.1063/1.323539.

Quaschning, V. V. 2019. *Renewable energy and climate change*. John Wiley & Sons.

Reddy, Y. K., V. Manjunath, S. Bimli, and R. S. Devan. 2022. Futuristic kusachiite solar cells of CuBi2O4 absorber and metal sulfide buffer layers: Theoretical efficiency approaching 28%. *Solar Energy* 244:75–83. doi: 10.1016/j.solener.2022.08.034.

Sarker, K., M. S. Sumon, M. Orthe, S. K. Biswas, M. M. Ahmed, and Q. Wang. 2023. Numerical simulation of high efficiency environment friendly CuBi 2 O 4-based thin-film solar cell using SCAPS-1D. *International Journal of Photoenergy* 2023:1–11. doi: 10.1155/2023/7208502.

Schieck, R., A. Hartmann, S. Fiechter, R. Könenkamp, and H. Wetzel. 1990. Electrical properties of natural and synthetic pyrite (FeS2) crystals. *Journal of Materials Research* 5 (7):1567–72.

Song, A., P. Plate, A. Chemseddine, F. Wang, F. F. Abdi, M. Wollgarten, R. van de Krol, and S. P. Berglund. 2019. Cu: NiO as a hole-selective back contact to improve the photoelectrochemical performance of CuBi 2 O 4 thin film photocathodes. *Journal of Materials Chemistry A* 7 (15):9183–94. doi: 10.1039/C9TA01489F.

Sullivan, I., B. Zoellner, and P. A. Maggard. 2016. Copper (i)-based p-type oxides for photoelectrochemical and photovoltaic solar energy conversion. *Chemistry of Materials* 28 (17):5999–6016.

Voigt, B., W. Moore, M. Manno, J. Walter, J. D. Jeremiason, E. S. Aydil, and C. Leighton. 2019. Transport evidence for sulfur vacancies as the origin of unintentional n-type doping in pyrite FeS2. *ACS Applied Materials and Interfaces* 11 (17):15552–63. doi: 10.1021/acsami.9b01335.

Wadia, C., A. P. Alivisatos, and D. M. Kammen. 2009. Materials availability expands the opportunity for large-scale photovoltaics deployment. *Environmental Science & Technology* 43 (6):2072–77. doi: 10.1021/es8019534.

Wang, F., A. Chemseddine, F. F. Abdi, R. van de Krol, and S. P. Berglund. 2017. Spray pyrolysis of CuBi 2 O 4 photocathodes: Improved solution chemistry for highly homogeneous thin films. *Journal of Materials Chemistry A* 5 (25):12838–47. doi: 10.1039/C7TA03009F.

Wu, N., Y. Wu, D. Walter, H. Shen, T. Duong, D. Grant, C. Barugkin, X. Fu, J. Peng, T. White, et al. 2017. Identifying the cause of voltage and fill factor losses in perovskite solar cells by using luminescence measurements. *Energy Technology* 5 (10):1827–35. doi: 10.1002/ente.201700374.